UC San Diego
Oceanography Program Publications

Title

Observations of runup and energy flux on a low-slope beach with high-energy, long-period ocean swell

Permalink

https://escholarship.org/uc/item/57x4g22b

Journal

Geophysical Research Letters, 42(22)

ISSN

00948276

Authors

Fiedler, Julia W
Brodie, Katherine L
McNinch, Jesse E
et al.

Publication Date

2015-11-28

DOI

10.1002/2015GL066124

Data Availability

The data associated with this publication are available upon request.

Peer reviewed

Observations of runup and energy flux on a low-slope beach with high-energy, long-period ocean swell

Julia W. Fiedler[1], Katherine L. Brodie[2], Jesse E. McNinch[2], and Robert T. Guza[1]

[1] Scripps Institution of Oceanography, University of California, San Diego, La Jolla, California, USA, [2] Coastal & Hydraulics Laboratory, U.S. Army Engineer Research and Development Center, Duck, North Carolina, USA

Abstract The transformation of surface gravity waves from 11 m depth to runup was observed on the low-sloped (1/80) Agate Beach, Oregon, with a cross-shore transect of current meters, pressure sensors, and a scanning lidar. Offshore wave heights H_0 ranged from calm (0.5 m) to energetic (>7 m). Runup, measured with pressure sensors and a scanning lidar, increases linearly with $(H_0 L_0)^{1/2}$, with L_0 the deep-water wavelength of the spectral peak. Runup saturation, in which runup oscillations plateau despite further increases in $(H_0 L_0)^{1/2}$, is not observed. Infragravity wave shoaling and nonlinear energy exchanges with short waves are included in an infragravity wave energy balance. This balance closes for high-infragravity frequencies (0.025–0.04 Hz) but not lower frequencies (0.003–0.025 Hz), possibly owing to unmodeled infragravity energy losses of wave breaking and/or bottom friction. Dissipative processes limit, but do not entirely damp, increases in runup excursions in response to increased incident wave forcing.

1. Introduction

Wave runup determines shoreline morphology change and can overtop dunes and damage coastal structures. Sea level rise and a potentially more energetic wave climate [e.g., *Cayan et al.*, 2008; *Bromirski et al.*, 2013] will increase the need to understand runup physics in energetic conditions.

Runup from monochromatic, normally incident waves saturates [*Miche*, 1951]. For a given incident wave period and beach slope, runup increases with increasing offshore incident wave height H_0, until reaching a maximum excursion. Further H_0 increases widen the surfzone but do not increase runup beyond this saturation level. Saturation concepts have been extended to the naturally occurring, broad-banded, and directionally spread spectra of incident waves. Observations suggest that runup saturation occurs at sea swell frequencies (nominally 0.04–0.25 Hz on ocean coasts) but that infragravity wave height at the shoreline (e.g., runup) is not saturated and continues to increase with increasing H_0 [e.g., *Huntley et al.*, 1977; *Guza and Thornton*, 1982; *Baldock and Holmes*, 1999; *Ruggiero et al.*, 2004; *Senechal et al.*, 2011; *Hughes et al.*, 2014, and others].

Infragravity waves (frequencies nominally 0.004–0.04 Hz) are generated by nonlinear interactions among sea swell waves. With sea swell of low height (e.g., 1 m), infragravity (hereafter IG) energy increases shoreward, with nearly complete shoreline reflection producing a standing wave [e.g., *Suhayda*, 1974]. With more energetic sea swell, shoreline reflection of IG energy decreases [*Sheremet et al.*, 2002], possibly owing to IG wave breaking [e.g., *de Bakker et al.*, 2014; *Battjes et al.*, 2004], shortwave breaking [*Baldock*, 2012], bottom friction [*Henderson and Bowen*, 2002], and/or energy transfer to shortwaves [e.g., *Henderson et al.*, 2006; *Thomson et al.*, 2006].

Recent field data from a steep beach with offshore $H_0 = 6.4$ m suggest IG saturation of runup and motivated a hyperbolic-tangent saturation fit of runup to incident wave heights [*Senechal et al.*, 2011]. IG saturation was also observed on a low-slope beach for $H_0 > 3$ m [*de Bakker et al.*, 2014]. However, the field observations are not conclusive, and numerical and laboratory modeling suggests that even with a wide surfzone, IG runup increases linearly with H_0 [*Ruju et al.*, 2014] without clear saturation. Runup in extreme conditions is understood poorly.

Here we present new observations on a low-slope beach, including detailed measurements of runup. IG energy fluxes and energy balances with ~7.1 m offshore wave heights show IG energy losses and transfer of IG energy to short waves across the wide surfzone (> 1 km). Although the hypothesized maximum runup excursion (fully saturated at all frequencies) is not reached, cross-shore IG energy fluxes suggest emergent IG saturation.
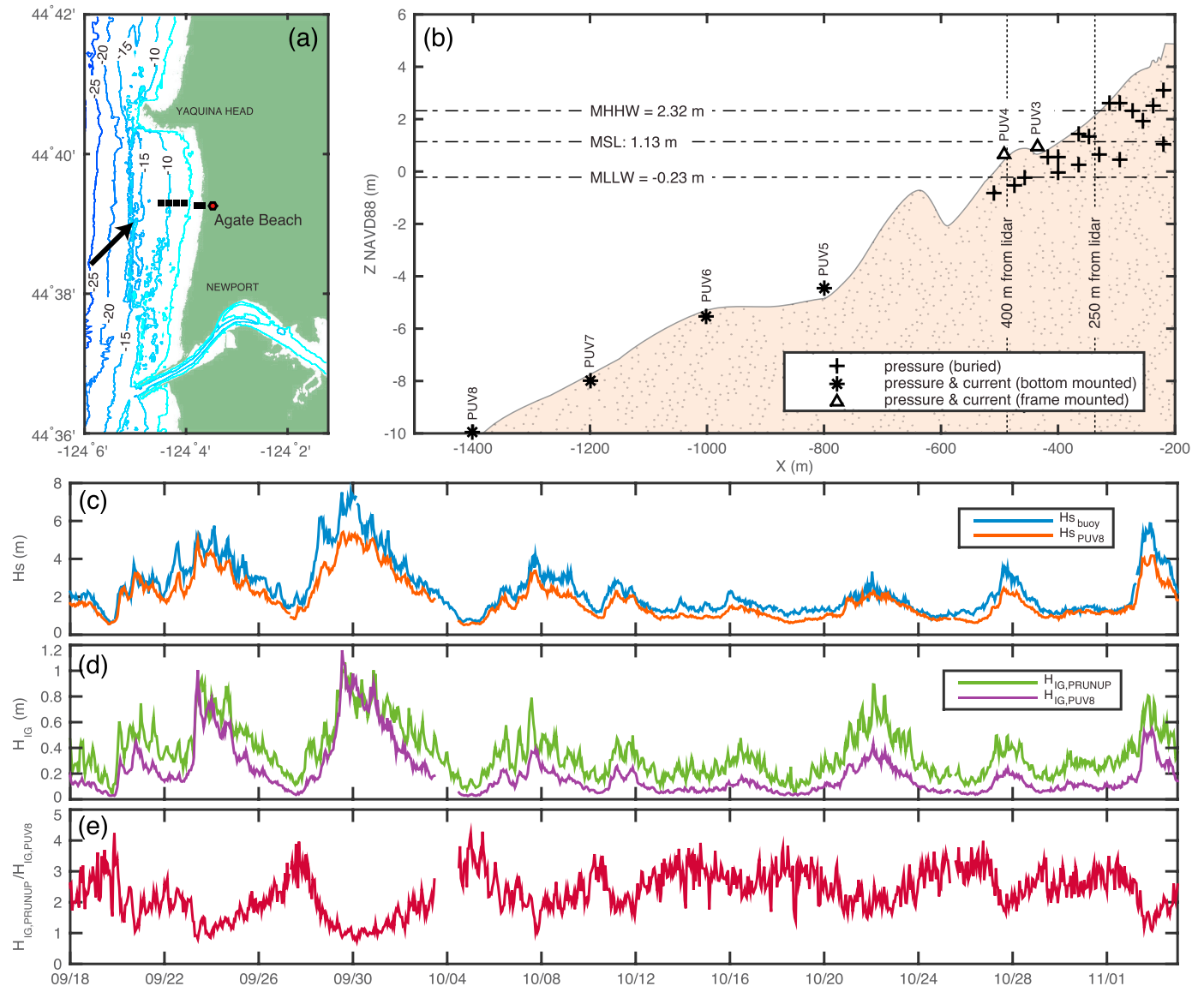
Figure 1. (a) Map of Agate Beach bathymetry (depths in m) with Lidar (red dot), and pressure and current meter (black dots) locations indicated. Arrow denotes an offshore ridge. (b) Depth and instrument locations versus cross-shore distance. Mean higher high (MHHW), mean (MSL), and mean lower lower (MLLW) water levels are indicated. Time series of (c) sea swell significant wave height at the offshore buoy (blue), PUV8 (in 11 m depth relative to MSL at the seaward edge of the array, red); (d) infragravity (IG) significant wave height at PUV8 (purple) and the seaward edge of the swash zone (runup proxy, green); (e) IG amplification or the ratio of IG-shoreline runup proxy relative to IG at the deepest sensor, (i.e., ratio of wave heights in Figure 1d).

2. Methods

2.1. Field Site

Observations were obtained at the low-slope (1:80), fine-grained (0.2 mm), Agate Beach in Newport, Oregon, from 19 September to 2 November 2013 (Figure 1). *Haxel and Holman* [2004] describe the geomorphology and geologic setting. Tidal ranges are 1.5 m (neap) and 3 m (spring). Energetic swell breaks on a rocky ridge, about 2 km offshore with 9 m crest depth (Figure 1a, arrow). The subaerial beach, surveyed with GPS Real Time Kinematic surveys at most low tides, changed little, except for a small (∼0.25 m) shoreward progressive perturbation in the swash zone in late October. The deeper sandbar location was stationary ($x \approx -650$ m, Figure 1b).

2.2. Waves and Currents

Water levels, waves, and runup were observed on a 1.2 km long cross-shore transect from the subaerial beach to about 11 m depth, relative to mean sea level (MSL) (Figure 1b). Eighteen pressure sensors, sampling at 2 Hz,
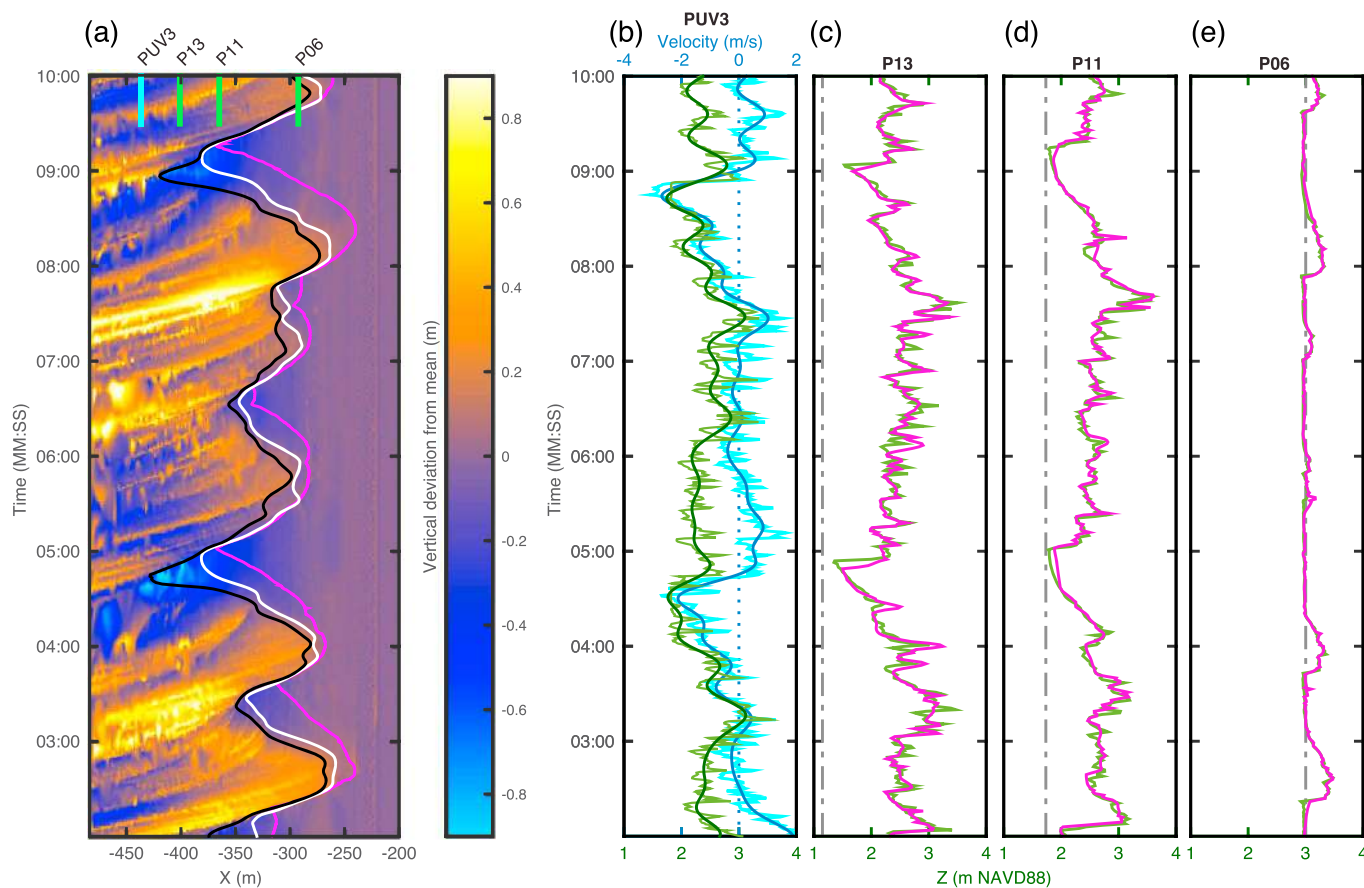
Figure 2. Time series spanning 8 min on 29 September, 22:00 PST; offshore buoy $H_0 = 7.49$ m, $T_p = 14.8$ s, $H_0 L_0 = 2562$ m^2. (a) Elevation on a cross-shore x transect versus time (i.e., vertically stacked lidar scans). The temporal mean at each x is removed by manually tracking runup fronts (purple) and using 10 cm and 20 cm edge depth thresholds (white and black, respectively). Pressure sensor locations are indicated on the top axis. (b) Inner surfzone (PUV3, $x = -434$ m, mean depth 2.5 m) cross-shore velocity (2 Hz, light blue; IG band passed, dark blue, $+u$ onshore) and pressure-derived sea surface elevation (2 Hz, light green; IG band passed, dark green). Sea surface elevation from (c) buried pressure sensors (green) and (e) lidar (magenta). The dashed line denotes the sand level at each sensor. IG energy is maximum ($H_{IG} \sim 1$ m) at (d) the pressure proxy P11, located at the seaward edge of the swash zone.

were located at elevations between -1 and 3 m NAVD88, spanning $\sim$300 m. Pressure sensors were buried to reduce exposure to debris and kelp, and to minimize flow effects, especially in the swash. Sea surface elevation spectra were estimated from pressure spectra using linear wave theory and poroelastic theory to account for burial [*Raubenheimer et al.*, 1998]. Two collocated pressure and current sensors (2 Hz sampling) were frame mounted (PUVs 3 and 4) between mean lower lower (MLLW) and mean higher high (MHHW) water levels, and four were bottom mounted between 5 and 11 m depth (PUVs 5–8). PUV data were rejected if the ratio of pressure to velocity variance in the sea swell band was outside the range 0.8–1.2 [*Herbers et al.*, 1999]. Offshore significant sea swell wave heights (National Data Buoy Center buoy 46050, located 37 km west of Newport in 128 m depth) varied between 0.5 and 7.5 m. Wave heights at the most offshore pressure sensor (PUV8 in 11 m depth) reached 5.5 m (Figure 1c). IG wave heights varied between 0.03–1.2 m at the most offshore pressure sensor and 0.05–1.1 m at the runup proxy pressure gauge (the shallowest pressure sensor with the maximum IG energy, Figure 1d). IG amplification, the ratio of significant IG wave heights at the shallowest surfzone pressure sensors relative to the deepest sensor, varied between 0.7 and 4.3. The largest offshore swell had the smallest IG amplification (Figure 1e).

2.3. Runup

A narrow-beam (0.3 mrad), 1550 nm wavelength lidar (Riegl VZ-1000) scanned the same cross-shore transect at 7 Hz for the first 50 min of each hour and measured the elevation of the subaerial beach and runup tongue with 0.02° angular resolution [*Brodie et al.*, 2015]. The distance from the lidar (located 33.3 m above MSL on a cliff top near $x = -88$ m, Figure 1a) to the waterline ranged from about 160 m (uprushes during high tide) to almost 500 m (downrushes during low tides). Scans were rectified using independently surveyed targets
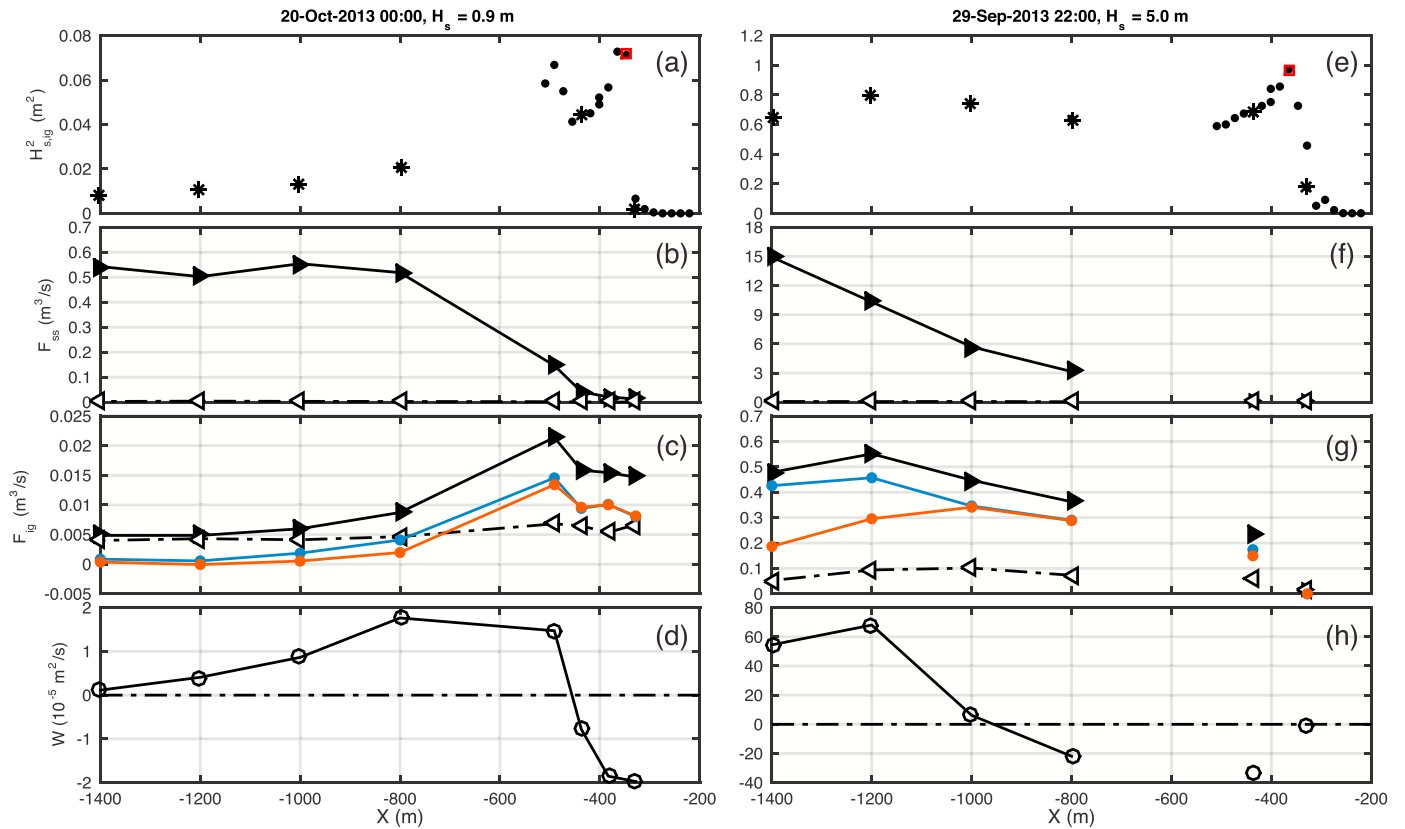
Figure 3. Contrasting 1 h records with (left) $H_0 = 0.9$ m (00:00, 20 October 2013) and (right) $H_0 = 5.0$ m (22:00, 29 September 2013) incident wave heights. Cross-shore evolution of (a, e) H_{IG}^2 derived from pressure at the PUV sensors (stars) and onshore pressure sensors (dots). Red symbol indicates the runup proxy pressure, where H_{IG}^2 is a local maximum; (b, f) Sea and swell (0.05–0.25 Hz) shoreward and seaward linear fluxes $F_{SS}^{\pm}$; (c, g) infragravity (0.003–0.04 Hz) shoreward and seaward linear fluxes $F_{IG}^{\pm}$ (arrow heads), with total linear (blue) and nonlinear (red) IG energy fluxes; (d, h) nonlinear IG energy transfer W. Note the different plot scales.

and coregistered hourly to an accurate baseline scan, accounting for movement of the lidar platform owing to solar heating and other effects. Lidar line scans (7.122 Hz) were gridded at 0.1 m cross-shore resolution [*Brodie et al.*, 2015], producing an $(x, t, \text{elevation})$ matrix (Figure 2a) visually similar to a video $(x, t, \text{intensity})$ "timestack" [e.g., *Stockdon et al.*, 2006].

Lidar data were noisy owing to the relatively long range (∼400 m compared with ∼70 m in *Brodie et al.* [2015]) and sometimes heavy wind, rain, and fog. To mitigate substantial noise, data were binned into a 1 m × 1 s grid of median values (Figure 2a). Processed lidar elevations agree well with water levels measured by buried pressure sensors (Figures 2c–2e). Runup time series were estimated from the lidar using 10 and 20 cm height thresholds (above the mean sand level) to define the leading edge of the runup tongue (Lidar 10 and Lidar 20, respectively). Selected hours were also processed manually from the noisier 0.1 m gridded data by visually determining the location of the runup toe and rundown, following the pixel intensity method of *Stockdon et al.* [2006] ("Lidar Front," purple line, Figure 2a). Rundown on the flat, often saturated lower foreshore was difficult to observe because the thin, mirror-like water layer during rundown was imaged poorly.

To supplement the lidar time series, a gap-free runup proxy was defined using the pressure sensor with the local maximum IG wave height for each hour (P11 in Figures 2, 3a, and 3e). At IG frequencies, Lidar Front, Lidar 10, Lidar 20, and proxy runup time series are mutually coherent with decreasing energy levels, due to the location of swash measurements (significant IG swash $S_{IG} = 1.7, 1.5, 1.4,$ and 1.0 m, respectively; Figure 2a). Different runup edge definitions correspond to different levels of immersion and thus erosion and flooding potential.

For each runup time series, vertical runup is estimated as [*Stockdon et al.*, 2006]

$$R_{2\%} = \langle \eta \rangle + \frac{S}{2}, \tag{1}$$

with setup $\langle \eta \rangle$ the time-averaged water level and S the significant swash height. At the proxy pressure sensor, significant IG wave height replaces S. Setup was measured with respect to the hourly mean water level at the deepest sensor (PUV8), where setup and setdown were usually small. However, during the most energetic events, error is introduced.

Stockdon et al. [2006] related $R_{2\%}$ to H_0L_0 derived from buoys in 10–15 m of water. The 11 m depth sensor is sometimes in the surfzone, reducing H_0 (30 September and 3 November in Figure 1c). Therefore, the offshore buoy (128 m depth) is used for offshore H_0L_0. *Ruggiero et al.* [2004] used offshore conditions in 64 m water depth at Agate.

2.4. Energy Flux Estimation

Shoreward and seaward infragravity energy fluxes (F^+ and F^-, respectively) were estimated from collocated pressure and cross-shore velocity measurements using linear shallow water theory [*Sheremet et al.*, 2002] as

$$F^\pm(f,x) = E^\pm(f,x)|C_x|. \tag{2}$$

with C_x as the cross-shore group speed and

$$E^\pm(f,x) = \frac{1}{4}\left(S_{PP}(f,x) + \frac{h^2}{C_x^2}S_{UU}(f,x) \pm 2\frac{h}{|C_x|}\Re\{S_{PU}(f,x)\}\right). \tag{3}$$

S_{PP} and S_{UU} are autospectra of IG-frequency P and U, respectively, and $\Re\{S_{PU}\}$ is the real part of the IG pressure-velocity cross spectrum (Figure 3). The net cross-shore flux, $F^+ - F^-$, depends only on the cospectrum, $h\Re\{S_{PU}\}$ (Figures 3c and 3e; blue line).

When reflection is weak, the net nonlinear IG energy flux (Figures 3c and 3e; red line) becomes [*Henderson et al.*, 2006]

$$F(f) = h\Re\{S_{PU}\} + \Re\{S_{PM}\} + \Re\{S_{S_{xx}U}\}. \tag{4}$$

The linear flux (first term on the right) is augmented with nonlinear corrections for a progressive wave involving wave mass flux M and radiation stress S_{xx}, where

$$M = \eta'u', \quad S_{xx} = \frac{h}{g}u'u' + \eta'\eta'/2. \tag{5}$$

The primed variables (u' and η') are band passed between 0.004 Hz and f_{up}, where f_{up}, where f_{up} is a high-frequency sea cutoff. IG frequencies are in M and S_{xx} to account for contributions from interactions among IG waves (important only at the shallowest sensors). In previous studies, $f_{up} = 0.4$ Hz [e.g., *Henderson et al.*, 2006; *Guedes et al.*, 2012]. Here f_{up} is a depth-dependent cutoff defined as the highest frequency (up to 0.4 Hz) at which the shallow-water wave number is equal to or greater than 75% of the finite-depth wave number. In 11 m depth, $f_{up} = 0.2$ Hz, increasing to a maximum of 0.4 Hz in shallow water.

The nonlinear energy transfer to IG frequencies is

$$W(f) = \Re\{S_{S_{xx},\partial U/\partial x}\}, \tag{6}$$

where W is a measure of work by the IG component of radiation stress on the IG strain. Positive (negative) W indicates a transfer of energy to (from) IG waves. With IG waves approximately shore normal and no energy loss from wave breaking and bottom friction (*Henderson et al.* [2006], following the derivations of *Phillips* [1977] and *Schäffer* [1993]),

$$W^{INT} = \Delta F. \tag{7}$$

The balance (7) assumes lowest-order IG and sea swell waves and includes resonant (and near-resonant) nonlinear interactions between IG waves, and between IG waves and sea swell waves. Phase coupling occurs owing to nonlinear interactions. Bound infragravity waves, not on the free wave dispersion curve, are neglected. W^{INT}, the nonlinear energy transfer integrated between two sensors, and ΔF, the change in the total nonlinear IG energy flux (4) between the two sensors, are compared below.

Vortical (eddy) motions are not associated with sea surface fluctuations, and contaminate the observations used in the long wave balance (7). Hours with Lippmann number (ratio of excess kinetic energy to potential energy at IG frequencies [*Lippmann et al.*, 1999]) greater than 0.2 were not analyzed, (approximately 50% of collected data hours). To adhere to the assumption of shore normal waves in (4), we reject data hours (near 60% of the data set) when the ratio of significant alongshore to cross-shore IG velocities (V_{IG}^2/U_{IG}^2, hereafter 2-D ratio) exceeds 0.4.
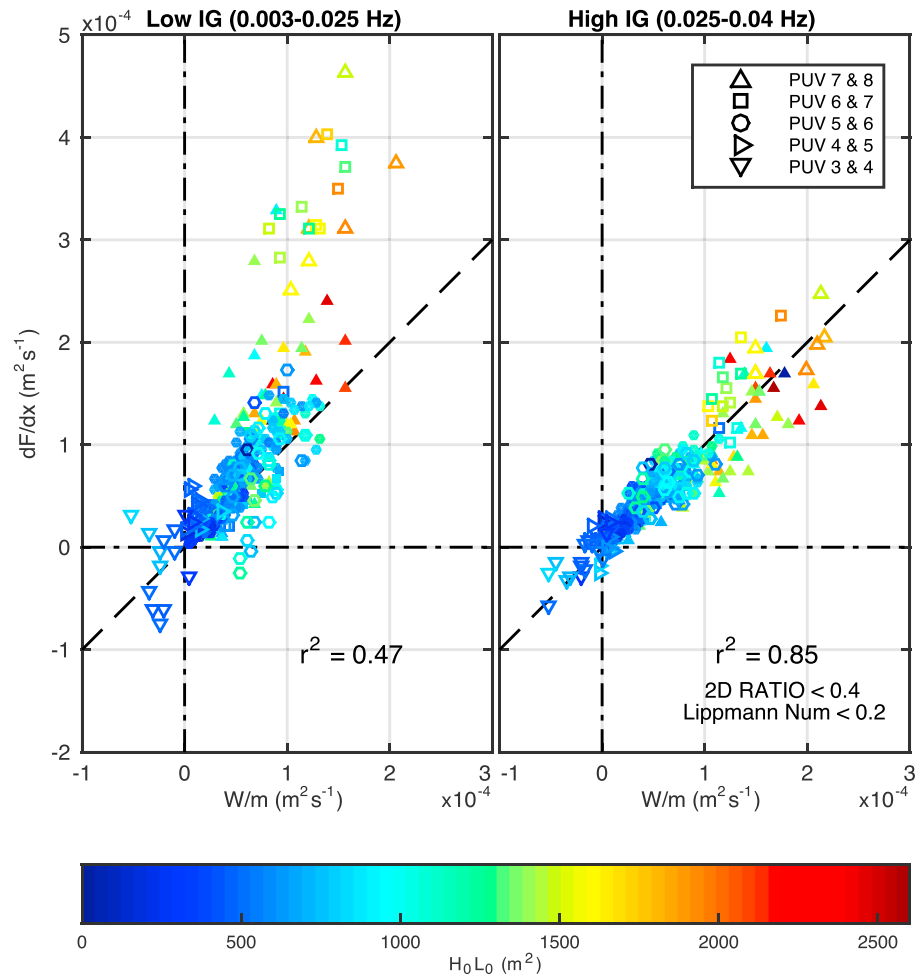
Figure 4. $\Delta F/\mathrm{d}x$ versus W^{INT}/m for (left) low-infragravity frequencies (0.004–0.025 Hz) and (right) high-infragravity frequencies (0.025–0.04 Hz). Sensor pairs are denoted by symbol. Breaking conditions, determined by a 20% loss of sea and swell energy over the sensor pair, are plotted in outlines, whereas nonbreaking conditions are filled. Color scaling represents the offshore wave conditions $H_0 L_0$. Only hours for which the Lippmann number is less than 0.2 and the cross-shore to alongshore energy flux (2-D) ratio is less than 0.4 are shown.

3. Results

3.1. Energy Fluxes

With low incident waves ($H_0 = 0.9$ m), H_s is maximum near the shoreline, at the seaward edge of the swash zone (Figure 3a). The net IG energy flux increases to a surfzone maximum ($x = 500$ m), with modest decreases at the shallowest sensors (Figure 3c). Nonlinear (red) and linear (blue) net fluxes are similar (Figure 3c).

With energetic waves ($H_0 = 5$ m), the entire array was in the shortwave surfzone (Figure 3f). The nonlinear IG energy flux (believed more accurate than the linear flux) was maximum in about 5 m depth ($x = -1000$ m in Figure 3g), with much reduced fluxes nearer the shoreline. The nonlinear IG flux is reduced almost tenfold from 0.3 m³/s at $x = -800$ m to about 0.03 m³/s at $x = -300$ m. The maximum H_{IG} is again at the outer edge of the swash zone (Figure 1e, but the maximum H_{IG} is only slightly larger than in 11 m depth ($x = -1400$ m). The cross-shore evolution of infragravity energy flux indicates a protosaturation of IG runup with large off-shore H_0. That is, the intensification of incident wave forcing (e.g., higher energy, longer swell, larger $H_0 L_0$), leads to a wider surfzone and increases the IG wave energy seaward of the surfzone but produces more modest increases or even decrease in the inner surfzone. Note that $W < 0$ in the inner surfzone with both high and low H_0 (Figure 3), indicating that nonlinear triad interactions are transferring energy from IG to sea swell (similar to *Henderson et al.* [2006] and *Thomson et al.* [2006]). However, the width of the $W < 0$ region is much less with small H_0.
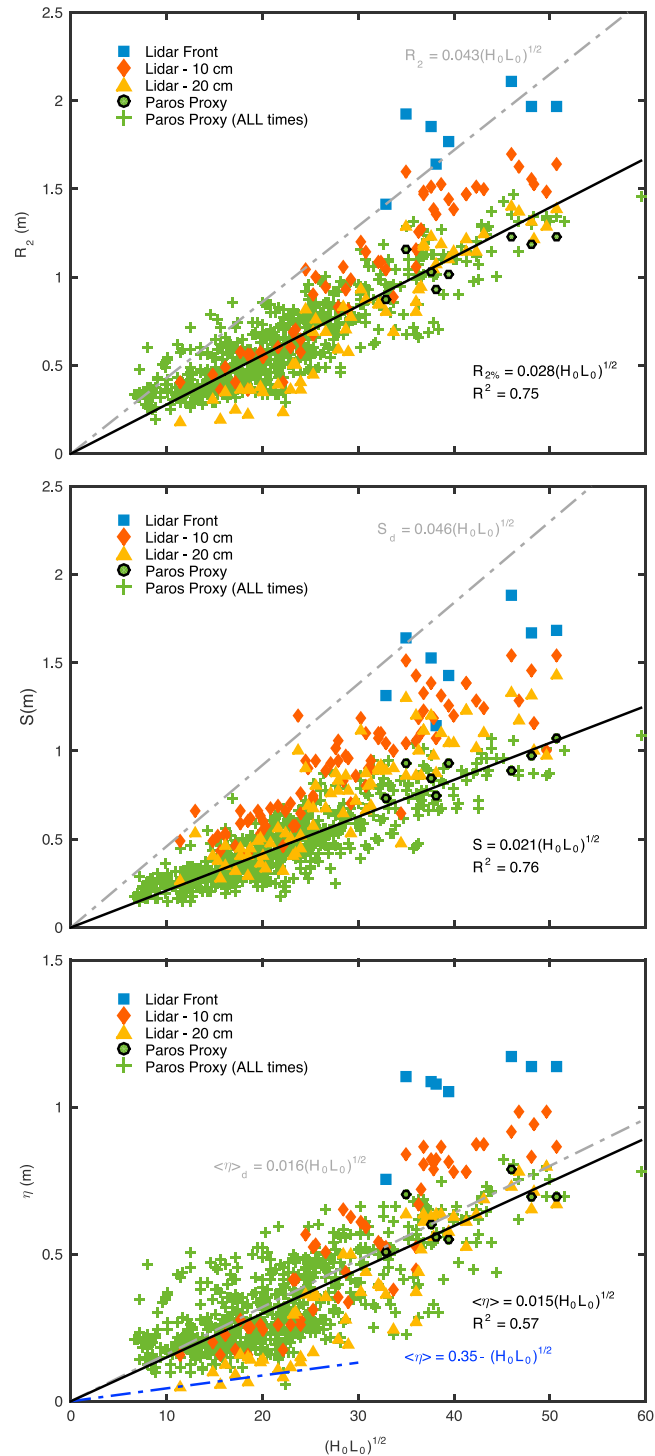
Figure 5. Observed runup (top) $R_{2\%}$, (middle) swash S, and (bottom) setup η, versus $(H_0L_0)^{1/2}$, following [*Stockdon et al.*, 2006]. Proxy runup elevations (green), determined from pressure sensor-derived water elevations, are always less than both types of lidar-derived elevations: an argus-like leading-edge tracker of the runup toe (blue squares, "Lidar Front"), water-depth-derived runup at 10 cm (red diamonds), and 20 cm (yellow triangles). In Figures 5 (top), 5 (middle), and 5 (bottom), the gray dashed line is the *Stockdon et al.* [2006] fit for each parameter for dissipative beaches ($\xi_0 < 0.3$), primarily based on front tracking. The solid black line is the best fit to runup proxy measurements. The blue dashed line in Figure 5 (bottom) is the suggested "global" fit for setup, irrespective of Iribarren number [*Stockdon et al.*, 2006].

To further examine protosaturation and IG energy loss, we compare the nonlinear energy transfer to/from IG frequencies (6) with the IG energy flux gradient between sensors (4), following *Henderson et al.* [2006]. The terms in the conservative energy balance (7) are normalized by distance to account for uneven sensor spacing ($\Delta F/dx$ versus W^{int}/m, Figure 4). High IG frequencies (0.025–0.04 Hz) better correspond to the theoretical energy balance than do low IG (0.004–0.025 Hz) frequencies ($r^2 = 0.87$ and $r^2 = 0.47$, respectively), even under breaking conditions (open symbols), defined here as a 20% loss of sea and swell energy over a sensor pair. Correlations did not change significantly by relaxing and tightening the assumptions of shore-normal propagation, excess rotational velocities, and modifying estimates of $\partial u/\partial x$ in (6).

The most notable deviation from a closed balance is at low IG frequencies at the deeper sensor pairs 6/7 and 7/8. With large $H_0 L_0$, the observed flux increases more rapidly (as much as twice as fast) than expected from nonlinear transfers alone (Figure 4, left). Similar excess energy flux has been attributed previously to both missing physics [*Henderson et al.*, 2006] and to errors associated with large instrument spacings degrading the W estimates (6) [*Pequignet et al.*, 2014].

It is clear that fluxes decrease dramatically in the inner surfzone with large $H_0 L_0$ (e.g., Figure 3g). However, the balance gradient terms (e.g., $\Delta F/dx$) often could not be estimated accurately with large $H_0 L_0$ because one of PUVs 3, 4, or 5 failed the test for rotational moments. In cases when PUV3 and PUV5 passed but PUV4 failed (e.g., Figure 3g), balances are not computed. The cases with the largest seaward decrease in nonlinear $\Delta F/dx$, possibly owing to $W < 0$ and unaccounted dissipation, are not shown in Figure 4. For the limited cases considered, the inclusion of IG triads improved the total conservative energy balance significantly ($r^2 = 0.47$ versus $r^2 = 0.35$ in low IG band), but had little effect on high IG band correlation increases slightly ($r^2 = 0.85$ versus $r^2 = 0.83$).

3.2. Runup

The best fit slope of runup proxy $R_{2\%}$ to $(H_0 L_0)^{1/2}$ is approximately 25% smaller than *Stockdon et al.* [2006] for dissipative ($\xi_0 < 0.3$) beaches (Figure 5, top). Many of the *Stockdon et al.* [2006] data sets use video "timestacks," with the leading edge of the runup toe determined by pixel intensity. A similar "intensity" method to find the leading edge in the lidar timestacks ("Lidar Front"), applied to a few selected hours, yielded values more similar to *Stockdon et al.* [2006].

While setup η is similar, the proxy swash term oscillation S is more than 50% smaller than that predicted by *Stockdon et al.* [2006] (Figures 5, middle and 5, bottom) using the Lidar Front on video timestacks. The proxy pressure sensor is by definition in deeper water than the runup toe, measuring infragravity waves before they surge up the beach face. Similarly, S for the leading-edge lidar runup (perhaps a few cm) are higher than the 10 and 20 cm depth cutoffs; the "shallower" instruments measure the largest swash excursions.

4. Discussion and Summary

Data collected at the low slope Agate Beach in Fall 2013 add valuable field measurements to the relatively sparse knowledge of wave runup in extreme conditions. Lidar and pressure sensors measured horizontal swash excursions as large as 140 m in high-energy conditions. Previous field data suggest saturation in infragravity frequencies for wave conditions similar to these [e.g., *Senechal et al.*, 2011; *de Bakker et al.*, 2014]. However, our observations show continued runup increase with increasing incident wave forcing, characterized as $(H_0 L_0)^{1/2}$. On the other hand, the amplification of IG motions at the shoreline relative to 1 km offshore (11 m depth) decreases dramatically during storms. If the amplification observed with low-energy incident waves also occurred with the most energetic incident waves, vertical shoreline runup would have been four times larger than observed.

On high-energy days, the entire array was in the surfzone even in 11 m water depth, suggesting that waves were breaking on the offshore ridge, ~2 km from shore (Figure 1a). Depth surveys and video showed nearshore bars closer to shore, implying that at times, there may have been three spatially distinct surfzones. A validated numerical model is required to understand IG generation on this complex bathymetry and the complex transition from protosaturation to full runup saturation.

References

Baldock, T. E. (2012), Dissipation of incident forced long waves in the surfzone—Implications for the concept of "bound" wave release at short wave breaking, *Coastal Eng.*, *60*, 276–285, doi:10.1016/j.coastaleng.2011.11.002.

Baldock, T. E., and P. Holmes (1999), Simulation and prediction of swash oscillations on a steep beach, *Coastal Eng.*, *36*(3), 219–242, doi:10.1016/S0378-3839(99)00011-3.

Battjes, J., H. J. Bakkenes, T. Janssen, and A. R. van Dongeren (2004), Shoaling of subharmonic gravity waves, *J. Geophys. Res.*, *109*, C02009, doi:10.1029/2003JC001863.

Brodie, K. L., B. Raubenheimer, S. Elgar, R. K. Slocum, and J. E. McNinch (2015), Lidar and pressure measurements of inner-surfzone waves and setup, *J. Atmos. Oceanic Technol.*, *32*, 1945–1959, doi:10.1175/JTECH-D-14-00222.1.

Bromirski, P. D., D. R. Cayan, J. Helly, and P. Wittmann (2013), Wave power variability and trends across the North Pacific, *J. Geophys. Res. Oceans*, *118*, 6329–6348, doi:10.1002/2013JC009189.

Cayan, D. R., P. D. Bromirski, K. Hayhoe, M. Tyree, M. D. Dettinger, and R. E. Flick (2008), Climate change projections of sea level extremes along the California coast, *Clim. Change*, *87*(S1), S57–S73, doi:10.1007/s10584-007-9376-7.

de Bakker, A., M. Tissier, and G. Ruessink (2014), Shoreline dissipation of infragravity waves, *Cont. Shelf Res.*, *72*, 73–82, doi:10.1016/j.csr.2013.11.013.

Guedes, R., K. R. Bryan, and G. Coco (2012), Observations of alongshore variability of swash motions on an intermediate beach, *Cont. Shelf Res.*, *48*, 61–74, doi:10.1016/j.csr.2012.08.022.

Guza, R. T., and E. B. Thornton (1982), Swash oscillations on a natural beach, *J. Geophys. Res.*, *87*(C1), 483–491, doi:10.1029/JC087iC01p00483.

Haxel, J. H., and R. A. Holman (2004), The sediment response of a dissipative beach to variations in wave climate, *Mar. Geol.*, *206*(1–4), 73–99, doi:10.1016/j.margeo.2004.02.005.

Henderson, S. M., and A. J. Bowen (2002), Observations of surf beat forcing and dissipation, *J. Geophys. Res.*, *107*(C11), 3193, doi:10.1029/2000JC000498.

Henderson, S. M., R. T. Guza, S. Elgar, T. H. Herbers, and A. J. Bowen (2006), Nonlinear generation and loss of infragravity wave energy, *J. Geophys. Res.*, *111*, C12007, doi:10.1029/2006JC003539.

Herbers, T. H., S. Elgar, and R. T. Guza (1999), Directional spreading of waves in the nearshore, *J. Geophys. Res.*, *104*(C4), 7683–7693, doi:10.1029/1998JC900092.

Hughes, M. G., T. Aagaard, T. E. Baldock, and H. E. Power (2014), Spectral signatures for swash on reflective, intermediate and dissipative beaches, *Mar. Geol.*, *355*, 88–97, doi:10.1016/j.margeo.2014.05.015.

Huntley, D. A., R. T. Guza, and A. J. Bowen (1977), A universal form for shoreline run-up spectra?, *J. Geophys. Res.*, *82*(18), 2577–2581, doi:10.1029/JC082i018p02577.

Lippmann, T. C., T. H. Herbers, and E. B. Thornton (1999), Gravity and shear wave contributions to nearshore infragravity motions, *J. Phys. Oceanogr.*, *29*(2), 231–239, doi:10.1175/1520-0485(1999)029<0231:GASWCT>2.0.CO;2.

Miche, A. (1951), Le pouvoir réfléchissant des ouvrages maritimes exposés à láction de la houle, *Ann. Ponts Chaussees*, *121*, 285–319, doi:10.1234/12345678.

Pequignet, A.-C. N., J. M. Becker, and M. A. Merrifield (2014), Energy transfer between wind waves and low-frequency oscillations on a fringing reef, Ipan, Guam, *J. Geophys. Res. Oceans*, *119*, 6709–6724, doi:10.1002/2014JC010179.

Phillips, O. M. (1977), *The Dynamics of Upper Ocean*, 2nd ed., Cambridge Univ. Press, New York.

Raubenheimer, B., S. Elgar, and R. T. Guza (1998), Estimating wave heights from pressure measured in sand bed, *J. Waterw. Port Coastal Ocean Eng.*, *124*, 151–154, doi:10.1061/(ASCE)0733-950X(1998)124:3(151).

Ruggiero, P., R. A. Holman, and R. A. Beach (2004), Wave run-up on a high-energy dissipative beach, *J. Geophys. Res.*, *109*, C06025, doi:10.1029/2003JC002160.

Ruju, A., J. L. Lara, and I. J. Losada (2014), Numerical analysis of run-up oscillations under dissipative conditions, *Coastal Eng.*, *86*, 45–56, doi:10.1016/j.coastaleng.2014.01.010.

Schäffer, H. A. (1993), Infragravity waves induced by short-wave groups, *J. Fluid Mech.*, *247*, 551–588, doi:10.1017/s0022112093000564.

Senechal, N., G. Coco, K. R. Bryan, and R. A. Holman (2011), Wave runup during extreme storm conditions, *J. Geophys. Res.*, *116*, C07032, doi:10.1029/2010JC006819.

Sheremet, A., R. T. Guza, S. Elgar, and T. H. Herbers (2002), Observations of nearshore infragravity waves: Seaward and shoreward propagating components, *J. Geophys. Res.*, *107*(C8), 3095, doi:10.1029/2001JC000970.

Stockdon, H. F., R. A. Holman, P. A. Howd, and A. H. Sallenger Jr. (2006), Empirical parameterization of setup, swash, and runup, *Coastal Eng.*, *53*(7), 573–588, doi:10.1016/j.coastaleng.2005.12.005.

Suhayda, J. N. (1974), Standing waves on beaches, *J. Geophys. Res.*, *79*(21), 3065–3071, doi:10.1029/JC079i021p03065.

Thomson, J. M., S. Elgar, B. Raubenheimer, T. H. Herbers, and R. T. Guza (2006), Tidal modulation of infragravity waves via nonlinear energy losses in the surfzone, *Geophys. Res. Lett.*, *33*, L05601, doi:10.1029/2005GL025514.